



Triggered ferroptotic polymer micelles for reversing multidrug resistance to chemotherapy



Min Gao^{a,1}, Jian Deng^{a,1}, Fang Liu^a, Aiping Fan^a, Yujuan Wang^a, Huiyuan Wu^a, Dan Ding^{b,c}, Deling Kong^{b,c}, Zheng Wang^a, Dan Peer^d, Yanjun Zhao^{a,*}

^a School of Pharmaceutical Science & Technology, Tianjin Key Laboratory for Modern Drug Delivery & High Efficiency, and Collaborative Innovation Center of Chemical Science and Engineering (Tianjin), Tianjin University, Tianjin, 300072, China

^b State Key Laboratory of Medicinal Chemical Biology (Nankai University), Tianjin, 300071, China

^c Key Laboratory of Bioactive Materials, Ministry of Education, College of Life Sciences, and Collaborative Innovation Center of Chemical Science and Engineering (Tianjin), Nankai University, Tianjin, 300071, China

^d Laboratory of Precision NanoMedicine, Department of Cell Research & Immunology, George S. Wise Faculty of Life Sciences, Department of Materials Sciences and Engineering, Iby and Aladar Fleischman Faculty of Engineering, Center for Nanoscience and Nanotechnology, and Cancer Biology Research Center, Tel Aviv University, Tel Aviv, 69978, Israel

ARTICLE INFO

Keywords:

Polymeric micelles
Drug delivery
Multidrug resistance
Ferroptosis
Redox homeostasis

ABSTRACT

Drug-tolerant persister cancer cells (PCCs) play an important role in the development of multidrug resistance (MDR) to anti-cancer drugs. This is due to the strong link between PCCs formation and epithelial-mesenchymal transition (EMT), as well as the low numbers of PCCs. In addition, PCC removal by traditional cytotoxic agents is poor due to the intrinsic high MDR activity in these cells. As a novel programmed cell death pathway, ferroptosis shows high potency to eliminate cells at the EMT state via manipulating intracellular redox homeostasis. The aim of this work was to utilize triggered ferroptotic polymer micelles for PCCs removal and MDR reversal both *in vitro* and *in vivo*. The micelles were made of arachidonic acid-conjugated amphiphilic copolymer that can enable rapid cargo release upon free radical-triggering in the tumor microenvironment. A potent ferroptotic inducer, RSL3 was encapsulated in the micelles to target the glutathione peroxidase 4 (GPX4). In the model resistant human ovarian adenocarcinoma cells, the RSL3 micelles were 30-fold more toxic than activatable control micelles due to the ferroptotic machinery. The lipid peroxidation-induced intracellular glutathione level reduction also made a contribution, which enhanced the potency of RSL3 for ferroptosis induction and enabled the drug-loaded micelles all-active. As an index of PCCs population, the level of CD133⁺ and aldehyde dehydrogenase (ALDH⁺) biomarker was significantly lower for the ferroptotic micelles in contrast to the control. The potency of ferroptotic micelles regarding PCCs reduction was proved by the *in vitro* soft agar colony forming assay. The *in vivo* anti-tumor efficacy of triggered micelles was further demonstrated in tumor-bearing nude mice in terms of PCCs biomarkers, tumor growth inhibition, mice survival, and GPX4 inhibition. This work demonstrates a novel strategy to overcome cancer MDR via the tailored ferroptotic micelles, which opens new avenues for managing resistant tumors.

1. Introduction

Efficient cancer treatment has been challenging because of the occurrence of multiple drug resistance (MDR) and the formation of metastasis [1]. MDR involves multiple mechanisms, among which the presence of persister cancer cells (PCCs) plays an important role [2,3]. PCCs are rare immortal cells within the tumor microenvironment that can self-renew by dividing and give rise to many cell types to constitute

the tumor stroma [3]. PCCs are found predominantly in a G₀, non-dividing cell cycle state, and hence can escape the conventional chemotherapies that target the fast proliferating cells [4,5]. Due to the above unique properties, PCCs have been postulated as one of the reasons of intrinsic drug resistance, leading to tumor relapse [6]. Accumulating evidence suggests a strong link between PCCs formation and epithelial-mesenchymal transition (EMT) that involves an increase in fibroid morphology and extracellular matrix components,

* Corresponding author. School of Pharmaceutical Science & Technology, Tianjin University, 92 Weijin Road, Nankai District, Tianjin, 300072, China.
E-mail address: zhaoyj@tju.edu.cn (Y. Zhao).

¹ M. Gao and J. Deng contributed equally.

invasiveness, and resistance to apoptosis [7]. PCCs support not only the primary tumor growth, but also the development of drug resistance and metastasis. Thus, effective elimination of PCCs is essential for developing novel therapies to prevent emergence of drug resistance and cancer relapse [3,8]. However, conventional chemotherapies often fail to eradicate cancer cells that have entered the PCC state, resulting in PCCs-mediated clinical relapse [9].

Compelling evidence has been gathered that ferroptosis, a particular cell death pathway, is capable to promote elimination of PCCs [10–12]. As a programmed cell death pathway, ferroptosis is dependent upon intracellular ferrous iron, but not other metals, and is morphologically, biochemically, and genetically distinct from apoptosis, necroptosis, and autophagy [13,14]. The ferroptotic process involves multiple steps, during which arachidonic acid (AA) and/or adrenic acid (AdA) are incorporated into phosphoethanolamine (PE), followed by the formation of two tailored lipid peroxides that act as the death signals to induce ferroptosis [15,16]. Nevertheless, the exact execution mechanisms that ultimately lead to cell death caused by the accumulation of tailored lipid peroxides are still unclear. Ferroptotic cell death can also be achieved by the reduction of intracellular glutathione (GSH) level and/or inhibition of glutathione peroxidase 4 (GPX4) that is the specific enzyme responsible for the repair of oxidized phospholipids [15].

There is a growing interest in utilizing ferroptosis mechanism to suppress tumor growth [17–19]. It has been demonstrated that PCCs in a high mesenchymal therapy-resistant cell state are dependent on the lipid hydroperoxidase GPX4 for survival [10]. The loss of GPX4 function results in selective ferroptotic death of PCCs *in vitro* and prevents *in vivo* tumor relapse in mice, suggesting that GPX4 targeting may be a therapeutic strategy to prevent acquired drug resistance [11]. An independent study revealed that a synthetic derivative of salinomycin, exhibited a potent and selective activity against breast PCCs both *in vitro* and *in vivo* by accumulating and sequestering iron to induce ferroptosis [12]. These phenomena are not restricted to limited cancer cell types and PCCs from many lineages subjected to diverse therapeutic regimens are selectively sensitive to ferroptosis in contrast to the parental cells [10]. Therefore, introducing ferroptotic cell death could be potentially used in a clinical setting to deplete the pool of PCCs and hence prevent tumor relapse.

Although ferroptosis is a drugable target, the currently available set of ferroptosis inducers suffer from an unfavorable pharmacokinetic profile and hence there is an urgent need for effective strategies to reach the threshold intra-tumor drug concentration and produce therapeutic benefits. Nanotechnology shows the benefit of drug solubilization, enhanced systemic circulation and passive tumor targeting *via* enhanced permeability and retention (EPR) effect [20–23]. Our recent work developed a novel type of all-active nanoscale micelles that contain unsaturated fatty acids [24]. Upon the triggering of reactive oxygen species (ROS), the peroxidation of fatty acids could induce the micelle disassembly and rapid cargo release. In addition, it was postulated that the process of lipid peroxidation could cause the reduction of intracellular glutathione (GSH), which would enhance the potency of ferroptosis to remove tumor cells. Since AA is a key precursor of ferroptosis, the integration of AA as a micelle building block would not only aid the induction of ferroptosis, but also enable the selectively rapid cargo release in the tumor site featured with high level of intracellular ROS. The presence of externally delivered AA would increase the intracellular level of ferroptosis-initiating precursor, i.e. AA-bearing phosphoethanolamine (PE-AA). The subsequent oxidation of PE-AA *via* either enzymatic or non-enzymatic approaches would boost the concentration of ferroptotic ‘death signal’, PE-AA-OOH, which could synergize with the action of RSL3. Therefore, the aim of this work was to employ triggered polymer micelles to load a typical ferroptotic inducer (RSL3) for efficient PCCs reduction and MDR reversal (Scheme 1). RSL3 induces ferroptosis *via* targeting GPX4. The amphiphilic polymer was made of methoxyl poly(ethylene glycol)-poly(lysine) (mPEG-PLys) with AA being covalently conjugated to the polymer side chains (Fig. S1,

Supporting Information). Doxorubicin (Dox)-resistant human ovarian adenocarcinoma cells (NCI/ADR-Res or NAR) were selected as the model cells.

2. Materials and methods

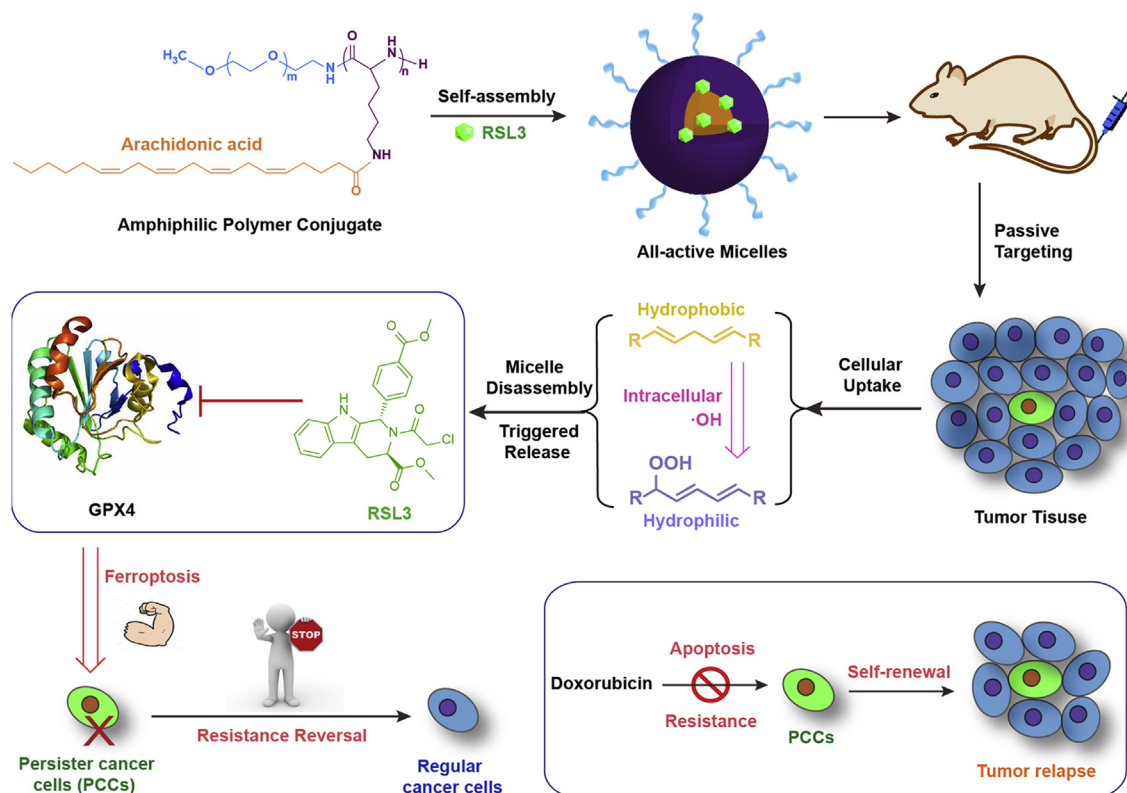
2.1. Materials

Methoxy poly(ethylene glycol) amine (mPEG-NH₂, 5000 Da) was purchased from JenKem Technology Co., Ltd. (Beijing, China). RSL3 and doxorubicin was purchased from Meilun Biotechnology Co., Ltd. (Dalian, China). LiperFluo was purchased from Dojindo laboratories (Kumamoto, Japan). Cy5 (SE) came from Bide Pharmatech Ltd. (Shanghai, China). RPMI 1640 cell culture medium, 2-Deoxy-D-glucose, PE-conjugated anti-CD133 antibody, mouse anti-human ALDH monoclonal antibody (5A11) and the corresponding secondary antibody goat anti-mouse IgG (H + L) (Alexa Fluor 555) were obtained from ThermoFisher (Shanghai, China). Anti-GPX4 antibody (ab125066), Rabbit anti human CD133 antibody (ab16518) and its corresponding secondary antibody donkey anti rabbit IgG (H + L) (Alexa Fluor 647) (ab150075) were purchased from Abcam (Shanghai, China). β -actin antibody and horseradish peroxidase (HRP)-labelled secondary antibody came from Shanghai Universal Biotech Co., Ltd. ALDEFLUOR kit was bought from Stem Cell Technologies (Beijing, China). Reduced glutathione (GSH) assay kit was purchased from Jiancheng Bioengineering Institute (Nanjing, China). MTT was bought from Sigma-Aldrich (Shanghai, China). Bradford protein assay kit and cellular glutathione peroxidase assay kit came from Beyotime Biotechnology Co. Ltd. (Shanghai, China). Low melting point agarose and crystal violet were bought from Solarbio (Beijing, China). The chemical solvents were sourced from Concord Technology Co. Ltd. (Tianjin, China) and the Gibco cell culture ingredients were bought from ThermoFisher (Shanghai, China). All other chemicals were obtained from Guangfu Fine Chemical Research Institute (Tianjin, China).

2.2. Micelles preparation and characterization

2.2.1. Drug loading and physicochemical assessment

The synthesis and preparation of amphiphilic AA-conjugated poly(ethylene glycol)-poly(lysine) polymeric micelle (mPEG-PLys-AA) utilized the method in our recent report [24]. The gel permeation chromatography (GPC) analysis employed tetrahydrofuran as the eluent and polystyrene as the calibration standard [24]. To obtain the RSL3-loaded micelles, 0.75 mg RSL3 together with 50 mg mPEG-PLys-AA were dissolved in CHCl₃ and mixed *via* vortexing and sonication. Then the organic solvent was gently evaporated to achieve a thin film that was subsequently hydrated with 10 mL deionized water, followed by sonication for 5 min. The excess RSL3 was removed by centrifugation and filtration through a 0.45 μ m membrane. Finally, the micelle solution was lyophilized and kept under argon at -20°C for further use. The cryoprotectant was not employed during lyophilization due to the stability of RSL3 and the difficulty of further purification post lyophilization. The RSL3 content in the micelles were analyzed by a high performance liquid chromatography (HPLC) (Waters e2695) coupled with a photo diode array (PDA) detector. In brief, the separation employed a Phenomenex C18 reverse phase column (Gemini) which maintained at 25°C . The mobile phase was a mixture of acetonitrile and 1% (v/v) acetic acid aqueous solution (60: 40, v/v) with a constant flow rate at 1 mL/min. The injection volume was 20 μ L and the detection wavelength was 230 nm. The hydrodynamic size and morphology of these polymeric micelles was analyzed according to standard protocols by a Malvern Zetasizer Nano ZS instrument and a JEM-100CX II transmission electron microscope, respectively. Ultraviolet-visible (UV-Vis) and Raman spectra were recorded by an Agilent Cary 60 UV-vis spectrophotometer and a RENISHAW inVia™ reflex confocal Raman micro spectrometer with the same test condition as published



Scheme 1. Schematic illustration of reactive oxygen species (ROS)-responsive polymer micelles for triggered delivery of RSL3, a model ferroptosis inducer. The polymer side chains contain unsaturated lipids that can transit from hydrophobic state to hydrophilic state upon lipid peroxidation, enabling rapid payload release. Traditional chemodrugs (e.g. doxorubicin) is impotent in eradicating persister cancer cells (PCCs) that are highly involved with multidrug resistance. RSL3 is presumed able to eliminate PCCs *via* targeting glutathione peroxidase 4 (GPX4) to reverse the multidrug resistance in antitumor therapy.

before [24].

2.2.2. Drug release *in vitro*

A set of static Franz diffusion cells which consist of donor chamber and receptor chamber were applied to study the drug release kinetics from the micelles. The donor chamber contained 2 mL micellar suspension in PBS (pH 7.4) and the receptor chamber was filled with pH 7.4 PBS buffer containing 5% (w/v) sodium dodecyl sulfate (SDS) and stirred by a magnetic bar. A regenerated cellulose membrane with a molecular weight cut-off (MWCO) of 2000 Da was clamped between two chambers. To mimic the disassembly behavior of AA-bearing micelles in cancer cells, the micellar PBS solution in the donor chamber was treated with FeCl_2 and H_2O_2 (both at 100 μM) to produce hydroxyl radical by Fenton reaction, whereas the control group was only dissolved in PBS. Finally, the collected samples at pre-determined time intervals were subjected to HPLC analysis for determining the extent of RSL3 release. All the measurements were performed at 37 °C and carried out thrice. At the same FeCl_2 and H_2O_2 concentration, the effect of hydroxyl radical incubation time (5, 10, 15, 20, and 30 min) on micelle stability was also determined using the hydrodynamic size and derived count rate as the indices [24].

2.2.3. Micelle stability

Regarding the plasma stability of RSL3-loaded micelles (Micelles/RSL3), the fluorescent intensity of RSL3 was monitored at pre-determined intervals, which could sensitively reflect the location of RSL3 (either micelles or medium). Micelles/RSL3 was dispersed in 10% (v/v) fetal bovine serum (FBS) containing PBS solution to mimic the *in vivo* condition. The final RSL3 concentration was 50 μM and the temperature was kept at 37 °C. The fluorescent intensities of RSL3 (F_t) were recorded with the excitation/emission wavelength at 280 nm/420 nm, respectively. The micelles stability was assessed by dividing F_t against the

corresponding fluorescence at 0 h (F_0). The kinetic fluorescence intensity ratio (F_t/F_0) was plotted against time.

2.3. Cell and animal model

Doxorubicin-resistant NCI-ADR/Res (NAR) human ovarian cancer cells were incubated in RPMI 1640 culture medium supplemented with 10% fetal bovine serum, 1% penicillin-streptomycin, and 1 × glucose at 37 °C containing 5% CO_2 . Female BALB/C nude mice were sourced from Huaifukang Bioscience (Beijing, China) and used according to the protocols approved by the Animal Ethics Committee of Tianjin University. The tumor model was established by subcutaneously injecting 3×10^6 NAR cells suspended in PBS (pH 7.4) into the axilla of each mouse. When the tumor volumes reach to 30–50 mm^3 the mice were ready for anti-tumor efficacy experiment.

2.4. Lipid peroxides detection

The intracellular lipid peroxides was detected using the LiperFluo probe that can selectively interact with lipid peroxides and emit intense fluorescence [25]. In detail, NAR cells were incubated in the 35 mm confocal plate at a density of 1×10^5 cells per plate. After 24 h's incubation, the cells were pre-stained with 10 μM LiperFluo for 30 min, followed by sample addition (free RSL3, activatable micelles, AA&RSL3, and micelles/RSL3). The concentration of RSL3 was fixed at 700 nM for free RSL3 and micelles/RSL3; the concentration of AA in activatable micelles and AA&RSL3 was set at 12.8 μM . After 5 h's incubation, the medium was removed and the cells were washed with PBS three times. The confocal imaging analysis was performed using a LSM-710 confocal laser scanning microscope (Carl Zeiss, Germany) with the excitation wavelength at 514 nm and the emission wavelength at 519–646 nm.

2.5. GSH detection

The standard GSH assay kit was utilized to detect the change of glutathione concentration post the treatment of free AA and AA-bearing micelles at different concentrations (180, 360, and 450 μM) as well as free RSL3 and RSL3-loaded AA-bearing micelles (RSL3 concentration: 10, 20, and 25 μM). In brief, 2×10^6 NAR cells were collected after 12 h's sample incubation. Then the harvested cells were suspended in 0.6 mL of PBS and sonicated for 5 min at 4 °C. Afterwards, 100 μL disrupted cell solution was then collected and mixed with 100 μL of reagent 1 of the GSH assay kit following by centrifuging at 3500 rpm/min for 10 min. The obtained supernatant was then mixed with the detection reagents of the assay kit based on the product protocol. The absorbance values at 405 nm were recorded by a SpectraMax microplate reader and the total protein content was determined by the Bradford protein assay kit.

2.6. GPX4 activity assay

GPX4 activity was measured by a commercial glutathione peroxidase assay kit. The NAR cells were treated by free RSL3, activatable micelles, AA&RSL3, micelles/RSL3 with the cells receiving no treatment as the control. The RSL3 concentration was fixed at 700 nM for free RSL3, micelles/RSL3, and AA&RSL3. The AA concentration was 12.8 μM for activatable micelles. After 12 h's treatment, the cells were harvested in PBS solution containing 0.2% (w/v) ethylenediaminetetraacetic acid (EDTA). Then, the GPX4 activity was detected according to the manufacturer's protocol. The absorbance at 340 nm was recorded every 1 min in a SpectraMax microplate reader with the temperature maintained at 25 °C.

We also employed Western blotting approach for assessing GPX4 activity. In brief, the lysate of formulation-treated NAR cells was collected for analysis. The protein level of these samples was quantified. Then these samples containing equal amount of protein (20 μg) was loaded and subjected to the standard SDS polyacrylamide gel electrophoresis. The proteins were separated at a constant voltage, followed by the electrical transfer to a 0.45 μm poly(vinylidene fluoride) PVDF membrane. Upon membrane blocking with 5% milk PBST (phosphate buffered saline with Tween 20) solution for 1 h at room temperature, the target proteins were incubated with GPX4-specific antibody and β -actin antibody overnight at a dilution of 1:2500 and 1:5000, respectively. The temperature was set at 4 °C. Thereafter, the HRP-conjugated anti-rabbit IgG H&L at a dilution of 1:5000 was applied as the secondary antibody and the specific bands were developed using ECL™ western blotting detection reagents. In terms of *in vivo* western blotting, the tumor tissues was excised and homogenized 48 h post the first intravenous dosing, followed by a similar approach of *in vitro* electrophoresis.

2.7. PCC biomarkers

2.7.1. In vitro assessment

As the CD133⁺ and ALDH⁺ phenotype can indicate cancer stem cell-like properties in NAR cells, e.g. enhanced differentiation, invasion, and resistance to chemotherapy, the *in vitro* flow cytometry analysis was employed to identify the CD133⁺ and ALDH⁺ subpopulation. In terms of flow cytometry analysis, the NAR cells were treated with free RSL3, AA&RSL3, activatable micelles and micelles/RSL3 for 24 h with an identical RSL3 concentration at 700 nM. The AA concentration in activatable micelles was 12.8 μM . The untreated NAR cells were used as the control. Then the cells were digested by trypsin, diluted and pipetted to single wells at a concentration of 1×10^6 cells/mL, followed by incubation with PE-conjugated anti-CD133 antibody for 1 h on ice. To label the ALDH, the cells were incubated with activated ALDEFUOR reagent for 45 min at 37 °C. Moreover, to identify the ALDH⁺ and ALDH⁻ subpopulations, a series of identical amount of cells were

incubated with the DEAB inhibitor as the control. After centrifugation, the collected cell pellets were re-suspended in the assay buffer provided in the ALDEFUOR kit and analyzed on a BD FACSCalibur™ flow cytometer.

2.7.2. In vivo assessment

Regarding the *in vivo* immunofluorescence staining, NAR tumor-bearing mice were intravenously injected with PBS, free RSL3, activatable micelles, AA&RSL3 and micelles/RSL3 using the same dose as that in the efficacy experiment. The tumors were collected at 48 h post dose administration and fixed in 4% paraformaldehyde for 1 h. Before making the frozen blocks, the tumor tissues were transferred to 30% sucrose solution and incubated overnight at 4 °C, followed by treatment with the Tissue-Tek® optimum cutting temperature (O.C.T.) compound, and freezing. Afterwards, the tumor tissue was cryo-sectioned to slices, marked with anti-CD133 and anti-ALDH antibodies, and subsequently stained with the corresponding secondary antibodies that were labelled with Alexa Fluor 647 and Alexa Fluor 555, respectively. The nuclear was stained by 4',6-diamidino-2-phenylindole (DAPI). Immunofluorescent images were photographed by an UltraView Vox confocal laser scanning microscope.

2.8. Cytotoxicity assay

The cytotoxicity measurement was quantified according to the standard MTT approach. The NAR cells were seeded in the 96-well plate with the density of 5×10^3 cells/well and incubated for 24 h. After that, free DOX, free AA, free RSL3, AA&RSL3, activatable micelles and micelles/RSL3 were added into each well at different concentration, respectively. After 24 h's incubation, the drug-containing culture medium was replaced with 100 μL MTT (0.5 mg/mL) solution. Four hours later, the MTT medium was replaced with 100 μL DMSO to dissolve the generated formazan. Finally, the absorbance at 490 nm was recorded by a microplate reader and the cell viability was calculated as the formula: $(\text{OD}_{490\text{sample}}/\text{OD}_{490\text{control}}) \times 100\%$.

2.9. Soft agar colony formation assay

Equal volume of $2 \times \text{RPMI 1640}$ medium and 1.2% low melting point agarose were thoroughly mixed and placed on the bottom of 6-well plate. Then, the plate was kept at 4 °C to obtain a 0.6% solidified agarose gel. Thereafter, NAR cells (1×10^4 /well) treated by free RSL3, AA&RSL3, activatable micelles and micelles/RSL3 (at three doses: 0.5, 1.0 and 1.5 IC_{50}) were separately mixed with 0.7% agar, followed by gentle transfer to 0.6% agarose coated-wells and subsequent solidification at ambient temperature for 15 min. The plates were incubated at an incubator containing 5% CO_2 at 37 °C for 16 days. Finally, the colonies were counted and imaged using an optical microscope.

2.10. Biodistribution

To track the biodistribution of the AA-conjugated micelles after intravenous injection, a fluorescent probe Cy5 was covalently linked to the backbone of mPEG-PLys-AA via amidation. In detail, 10 mg of Cy5 SE were mixed with mPEG-P(Lys-AA) (100 mg) polymer in 10 mL DMF. After stirring for 24 h at room temperature, the solution was dialyzed against water (MWCO: 3500 Da) and finally freeze-dried to obtain dark blue powder. The Cy5 content was quantified by a fluorescence spectrophotometer with the $E_x = 647 \text{ nm}$ and $E_m = 670 \text{ nm}$. Then the free Cy5 and Cy5-labelled mPEG-P(Lys-AA) polymeric micelles (Cy5: 20 $\mu\text{g}/\text{mL}$, 100 μL) were intravenously injected via the tail vein ($n = 3$). The kinetic fluorescence distribution at 2 h, 4 h, 6 h, 8 h, and 24 h were photographed using a Cri Maestro living imaging instrument (Cambridge Research & Instrumentation, Inc., MA, USA). Moreover, the mice were euthanized at 24 h post administration and the major organs and tumors were excised to see the *ex vivo* fluorescence distribution.

2.11. *In vivo* efficacy

For tumor inhibition analysis, the NAR tumor-bearing mice were randomized divided into five groups with six mice in each group. Each mouse received intravenous injection of formulations (100 μ L) every four days for a total of 3 times of dosing. The test formulations include PBS, free RSL3, AA&RSL3, activatable micelles, and micelles/RSL3 (RSL3 dose: 1.28 mg/kg, activatable micelles dose = 113.5 mg/kg). The tumor volume was measured every two days and was defined as the formula: $V = (L \times W^2)/2$, where L is the tumor length and W is the tumor width. The relative tumor volume was calculated according to the equation: V/V_0 (V_0 is the initial tumor volume before the start of treatment). The body weight of mice was measured to evaluate the systemic toxicities. Then, 36 days later, the mice were euthanized and the major healthy organs and the tumor tissues were excised for histological examination following the standard hematoxylin and eosin (H & E) staining protocols. Regarding the survival analysis, the NAR tumor-bearing mice that received triple dosing were continually monitored, recorded, and euthanized when reaching the humane endpoints.

2.12. Statistical analysis

The data were manipulated as average plus/minus standard deviation. Statistical comparison between different samples employed either Student's t-test or analysis of variance coupled with Tukey's post-hoc analysis. The threshold p value was set at 0.05.

3. Results and discussion

3.1. Triggered micelles: drug loading and release

The self-assembly of amphiphilic polymer in aqueous medium has been a robust approach to produce multifunctional pharmaceutical micelles [26]. In the current work, PEG was selected as the hydrophilic block of polymer, which was almost the golden standard for micelle manufacture [27]. Biocompatible polypeptide was used as the multi-valent hydrophobic backbone [28,29], where AA was picked up as the side chains to tailor the amphiphilic polymer conjugate. The reason to select AA as the conjugate building block was because it showed a high hydrophobicity ($\text{Log } P = 6.3$) and contained multiple double bonds for the ease of peroxidation-triggered cargo release [24]. The average conjugate molecular weight was ca. 7400 Da with a mean conjugation degree of 40%; the GPC analysis of polymer conjugate showed the weight average molecular weight (M_w), number average molecular weight (M_n), and polydispersity index (PDI) was 9600 Da, 8700 Da, and 1.1 [24]. The obtained conjugate successfully assembled into spherical micelles in aqueous medium. Prior to lyophilization, the hydrodynamic size of activatable micelles was within nanorange (control micelles: 70.3 ± 10.9 nm, PDI: 0.15 ± 0.03) and the size of micelles slightly increased upon cargo loading (micelles/RSL3: 90.1 ± 18.5 nm, PDI: 0.19 ± 0.05) (Fig. 1A). Post lyophilization, the hydrodynamic size marginally increased for both samples (control micelles: 78.6 ± 17.2 nm, PDI: 0.21 ± 0.05 ; micelles/RSL3: 95.7 ± 22.6 nm, PDI: 0.22 ± 0.06). For all types of micelles, the transmission electron microscope (TEM) size of micelles was relatively smaller than the corresponding hydrodynamic diameter (Table S1, Supporting Information).

The RLS3 loading was determined at $1.3 \pm 0.2\%$ in micelles with a corresponding encapsulation efficiency of $86.7 \pm 6.7\%$ post physical cargo loading. This value was in good agreement with previous report on non-covalent nanoencapsulation approaches, i.e. $< 5\%$ [30]. The drug-loaded micelles/RSL3 displayed decent stability in a biological medium with the aid of intrinsic cargo fluorescence (Fig. 1B). To focus on the interaction between micelles and plasma under static conditions, no agitation was applied for the *in vitro* stability assessment. The RSL3 release was carried out at physiological temperature using the static

Franz cell under sink conditions with the aid of a surfactant as the solubilizer. The cytoplasmic pH (7.4) was employed in the release study because of the intracellular ferroptosis execution that involved three hallmarks including Fe^{2+} , tailored lipid peroxidases, and GPX4 function impairment. It was clear that ROS treatment could significantly enhance drug release, which was believed as the hydroxyl radical-triggered AA peroxidation and subsequent micelle disassembly (Fig. 1C). Under the current experimental settings, the produced hydroxyl radicals did not affect the buffer pH as a consequence of the large concentration gap (2000 times) between the hydroxyl radicals and buffering ingredients. The relatively low extent of drug release was a consequence of the nature of Franz cell methodology for drug release test and the poor aqueous solubility of RSL3 ($\text{Log } P = 3.5$) that presents additional rate-limiting step [31].

We employed a combination of ferrous iron and hydrogen peroxide (100 μ M) for *in situ* generation of hydroxyl radical by taking advantage of the Fenton reaction. Hydroxyl radical is a type of highly potent ROS. Its incubation with activatable micelles for 30 min induced a dramatic change of micelles' ultraviolet-visible (UV-vis) spectra, which was presumed as a result of ROS-induced AA peroxidation (Fig. 1D). The Raman spectra further verified the oxidation of AA upon hydroxyl radical treatment (Fig. 1E). The AA moiety usually display a manifest band at 3015 cm^{-1} due to the stretching of $=\text{C}-\text{H}$ bond [32]; upon ROS treatment for 30 min, this unique band almost disappeared due to the loss of $\text{C}=\text{C}$ bonds. The AA oxidation process generated hydrophilic peroxidation products, which changed the amphiphilicity of conjugates and led to disassembly or expansion of micelles. In the current work, this was reflected by the increase of micelles' hydrodynamic size with extended incubation with hydroxyl radical (Fig. 1F). Meanwhile, the derived count rate (DCR) of micelles decreased accordingly to coincide with the micelle expansion (Fig. 1F) [33]. DCR is a calculated parameter in dynamic light scattering analysis and is representative of the scattering intensity in the absence of laser attenuation filter. DCR usually decreases upon particle expansion or aggregation, which has been used as an index for assessing nanoparticle stability [33].

3.2. Lipid peroxidation-induced GSH depletion

As expected, the supplement of both free AA and AA-bearing micelles successfully provoked the depletion of intracellular GSH at an AA dose-dependent manner (Fig. 2A). However, free RSL3 did not induce appreciable GSH depletion, which was consistent with previous publications [34,35]. The tumor cells are well characterized with the elevated level of ROS [36,37]. These ROS could trigger a cascade event of AA peroxidation, further increase the ROS concentration, and produce aldehyde end-products [24,38]. As the major antioxidant inside the cells, GSH would fight against the boosted ROS in attempt to maintain the redox hemostasis, leading to increased accumulation of glutathione disulfide (GSSG) that was accompanied with the exhaustion of GSH. At the same lipid concentration, free AA was more potent in depleting GSH than its micellar counterpart, which was presumed partly due to the different extent of cellular uptake. GPX4 could catalyze the reduction of lipid peroxides, which was accompanied with the transition of GSH to GSSG. The GPX4 activity was indirectly reflected by the decrease of nicotinamide adenine dinucleotide phosphate (NADPH)'s absorbance at 340 nm. Therefore, it was anticipated to see the reduction of NADPH for cells treated by AA-bearing activatable micelles, which was analogous to the control without any treatment (Fig. 2B). GPX4 is a major lipid repair enzyme, and the results demonstrated that the RSL3-free micelles did not cause the activity loss of GPX4. However, for all the other three samples containing RSL3 (i.e. free RSL3, micelles/RSL3, and AA&RSL3), the intracellular NADPH almost kept constant, indicating no variation of GPX4 activity (Fig. 2B). Likewise, the Western blot images showed a clear GPX4 inhibition for AA&RSL3 and micelles/RSL3 in contrast to other RSL3-free samples (Fig. 2C). This can be easily explained by the action mechanism of RSL3 as a powerful GPX4 inhibitor [9,13].

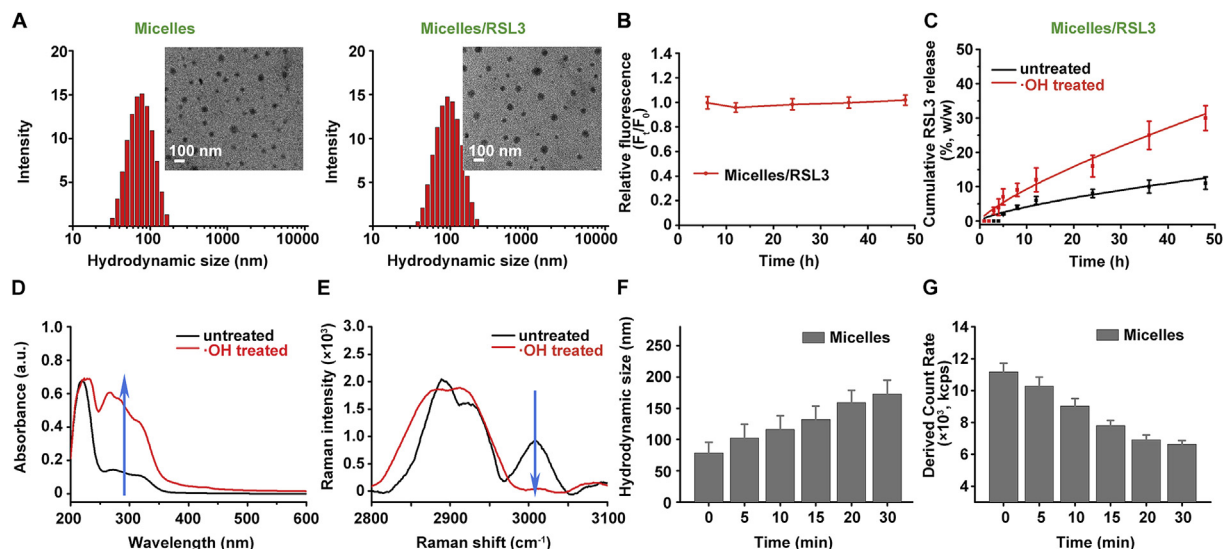


Fig. 1. Physicochemical assessment of drug-loaded all-active micelles. (A) Hydrodynamic and representative transmission electron microscope size (scale bar: 100 nm) of activatable micelles, RSL3-loaded micelles (*i.e.* Micelles/RSL3); (B) Plasma stability of RSL3-loaded micelles based on a fluorescent approach ($n = 3$); (C) Cumulative drug release from Micelles/RSL3 micelles with or without hydroxyl radical treatment ($n = 3$); (D) Ultraviolet–visible spectra and (E) Raman spectra of activatable micelles with and without hydroxyl radical treatment; Influence of hydroxyl radical incubation time on the (F) hydrodynamic size and (G) derived count rate of activatable micelles ($n = 3$).

3.3. Lipid peroxides accumulation

We employed a fluorescent probe (LiperFluo) for selective lipid peroxides detection and imaging [25]. LiperFluo is a small molecular conjugate of oligooxyethylene and a perylene derivative. It was not surprising to observe the presence of lipid peroxides in the NAR cells without any formulation treatment (control) due to the elevated ROS level in cancer cells (Fig. 3A). RSL3 could inhibit the function of GPX4, resulting the loss of lipid repairing ability and hence the accumulation of lipid peroxidation products. The AA-bearing activatable micelles

could boost the intracellular level of lipid peroxides *via* directly supplementing the unsaturated lipids. The cells treated by micelles/RSL3 or AA&RSL3 displayed the highest level of lipid peroxides due to the GPX4 inhibition together with AA supply (Fig. 3B and C). The capacity of AA-bearing Activatable micelles in ROS boosting together with concurrent GSH depletion makes it an ideal “all-active” nanoplatform in delivering ferroptosis-inducing agents for maximizing the therapeutic outcomes.

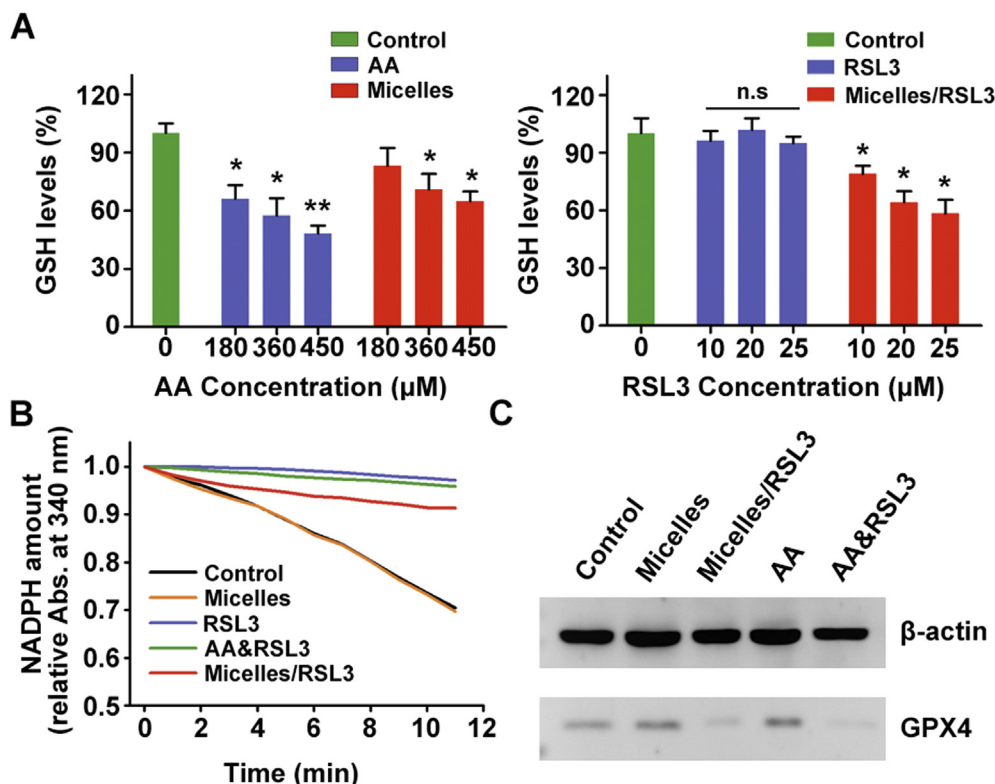


Fig. 2. The effect of lipid peroxidation on the intracellular glutathione (GSH) concentration and glutathione peroxidase 4 (GPX4) activity in NAR cells. (A) Dose-dependent GSH depletion: (*left*) free AA, and AA-bearing Activatable micelles; (*right*) free RSL3 and RSL3-loaded micelles (*n.s.* not significant; $*p < 0.05$, $**p < 0.01$, $n = 3$); the cells without any sample treatment were used as the control; (B) Intracellular GPX4 activity assay in cells with no treatment (control), and those treated by AA-bearing Activatable micelles, free RSL3, micelles/RSL3, and the physical mixture of AA and RSL3 (data are presented as the relative reduction of NADPH absorption at 340 nm); (C) Western blotting analysis of GPX4 in NAR cells post five different sample treatment.

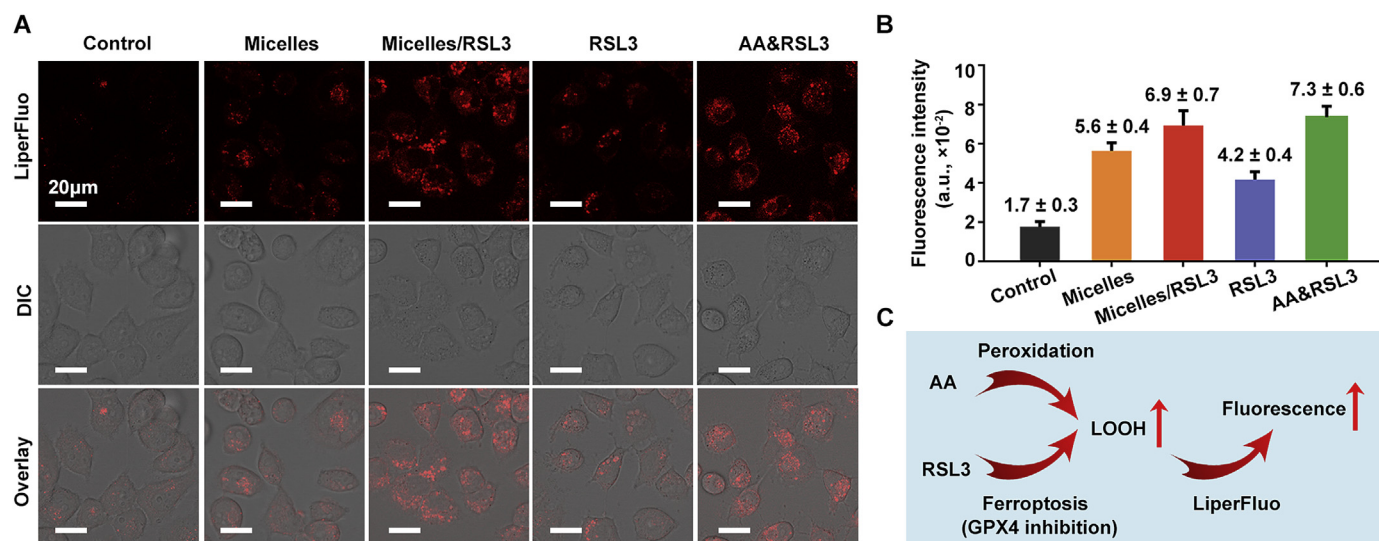


Fig. 3. Fluorescent detection of lipid peroxides in NAR cells by LiperFluo. (A) Confocal microscope images of NAR cells treated by activatable micelles, free RSL3, AA & RSL3, and micelles/RSL3; the cells without any sample treatment were used as the control (scale: 20 μm); (B) Quantitative summary of LiperFluo fluorescence intensity in five different samples ($n = 3$); (C) Illustration of the synergism of arachidonic acid (AA) and RSL3 in producing lipid peroxides that can be detected by LiperFluo.

3.4. Ferroptosis-induced PCCs depletion and cytotoxicity *in vitro*

PCCs primarily stay in the non-dividing and quiescent G_0 phase. Hence the silent PCCs are inherently resistant to traditional apoptosis-based chemotherapies, which eventually leads to tumor relapse and metastasis via the self-renewal and differentiation of PCCs into multiple types of tumor cells [39,40]. As a unique programmed cell death mechanism, ferroptosis targets the intracellular redox homeostasis, which is not dependent on the status of cell cycle [13,14]. Namely, ferroptosis is capable of reducing PCCs, which opens one potential avenue for addressing the drug resistance problem in conventional chemotherapy. The subpopulation of CD133^+ and ALDH^+ cells has been used as reliable biomarkers to assess the amount of PCCs in cancer cells [41,42]. It was apparent that the PCCs population in NAR cells treated by micelles/RSL3 dramatically decreased compared to the control in terms of both CD133^+ and ALDH^+ subpopulations (Fig. 4). Activatable micelles almost displayed negligible effect on PCCs suppression. The free drug (AA&RSL3 or RSL3) was superior regarding PCCs reduction than its micellar counterpart at the same dose, which was presumed due to the necessity of cargo release for micelles and the difference in cellular uptake. AA&RSL3 also had a slightly better performance than RSL3 alone because the presence of AA contributed to the elevation of lipid peroxides and hence the enhancement of ferroptosis potency. These results demonstrated that the potent GPX4 inhibitor RSL3 could ultimately address the drug resistance problem and increase the therapeutic anti-cancer efficacy via ferroptotic cell death pathway.

We employed the routine 3-(4,5-dimethylthiazol-2-yl)-2,5-diphenyltetrazolium bromide (MTT) assay to analyze the cytotoxicity of different formulations in NAR cells [43]. Unsurprisingly, NAR cells showed high resistance to free DOX treatment and a high dose at 100 μM only resulted in a 70% cell viability (Fig. S2, Supporting Information), the corresponding half maximal inhibitory concentrations (IC_{50}) was almost two orders higher than that in other non-PCC cancer cells [44,45]. Both free AA and activatable AA-bearing micelles displayed a lipid dose-dependent cytotoxicity ($p > 0.05$), as a consequence of lipid peroxides production and GSH depletion (Fig. 5A and Fig. 2A). Free RSL3 showed a high cytotoxicity to NAR cells due to its potent ability in inhibiting GPX4; the combination of RSL3 and AA at the free form seemed able to enhance the cytotoxicity because of simultaneous GPX4 inhibition and increase of lipid peroxides concentration (Fig. 5B). The micellar formulations were more potent than

the free drug, owing to the contribution of micellar nanocarrier as an “all-active” delivery vehicle (Fig. 5B). The IC_{50} of all formulations was summarized in Table S2 (Supporting Information). The *in vitro* cell viability assay demonstrated that the ferroptosis induction showed high cytotoxicity to resistant NAR cells.

To demonstrate the involvement of PCCs elimination in ferroptotic micelles-induced cytotoxicity, the standard *in vitro* clonogenic assay (or colony formation assay) was performed [46]. Because only a small fraction of seeded cancer cells retains the capacity to produce colonies, the clonogenic activity can be used as an indicator of undifferentiated PCCs after therapeutics treatment [47,48]. Since PCCs possess the capabilities of self-renewal, differentiation, and tumorigenicity, the removal of this small subpopulation of cells would restrain cancer cell growth. In the current work, all three ferroptotic formulations (micelles/RSL3, free RSL3, and AA&RSL3) effectively reduced the colony formation of NAR cells in a dose-dependent manner (Fig. 5C and Fig. S3, Supporting Information). On the contrary, the diminishment of colony formation was not observed with increasing dose supplement for NAR cells treated by negative control or activatable micelles. Such behavior can be explained by the ferroptosis-induced PCCs removal and hence the compromised initiation of cancer cell growth [48]. These data also concurred well with the PCCs biomarker analysis upon ferroptotic sample treatment.

3.5. Systemic delivery of micelles/RSL3 accumulates in tumor tissue

Herein, because the micelles did not display intrinsic fluorescence, a fluorescent probe (Cy5) was used to label the micelles with free Cy5 as the control [49]. Following intravenous administration of Cy5-labelled micelles, the micelles showed a kinetic tumor deposition profile that reached the peak at 8 h post injection (Fig. 6A and C). The extent of micelles accumulation in tumors was significantly higher than the free Cy5 control that was lack of EPR-based passive tumor targeting ability [50]. Due to the non-specific biodistribution, both samples also existed in other major healthy organs, e.g. heart, liver, spleen, lung, and kidney. At 24 h post micelles administration, Cy5 signal was significantly higher in the tumor compared to the free probe control (Fig. 6B and D).

The PEGylated micellar nanocarriers often show long systemic circulation [26]. After circulation in the blood, the deposition of micelles in the tumor site is the first step, followed by tumor penetration, cellular uptake, endosomal escape, drug release prior to exerting a

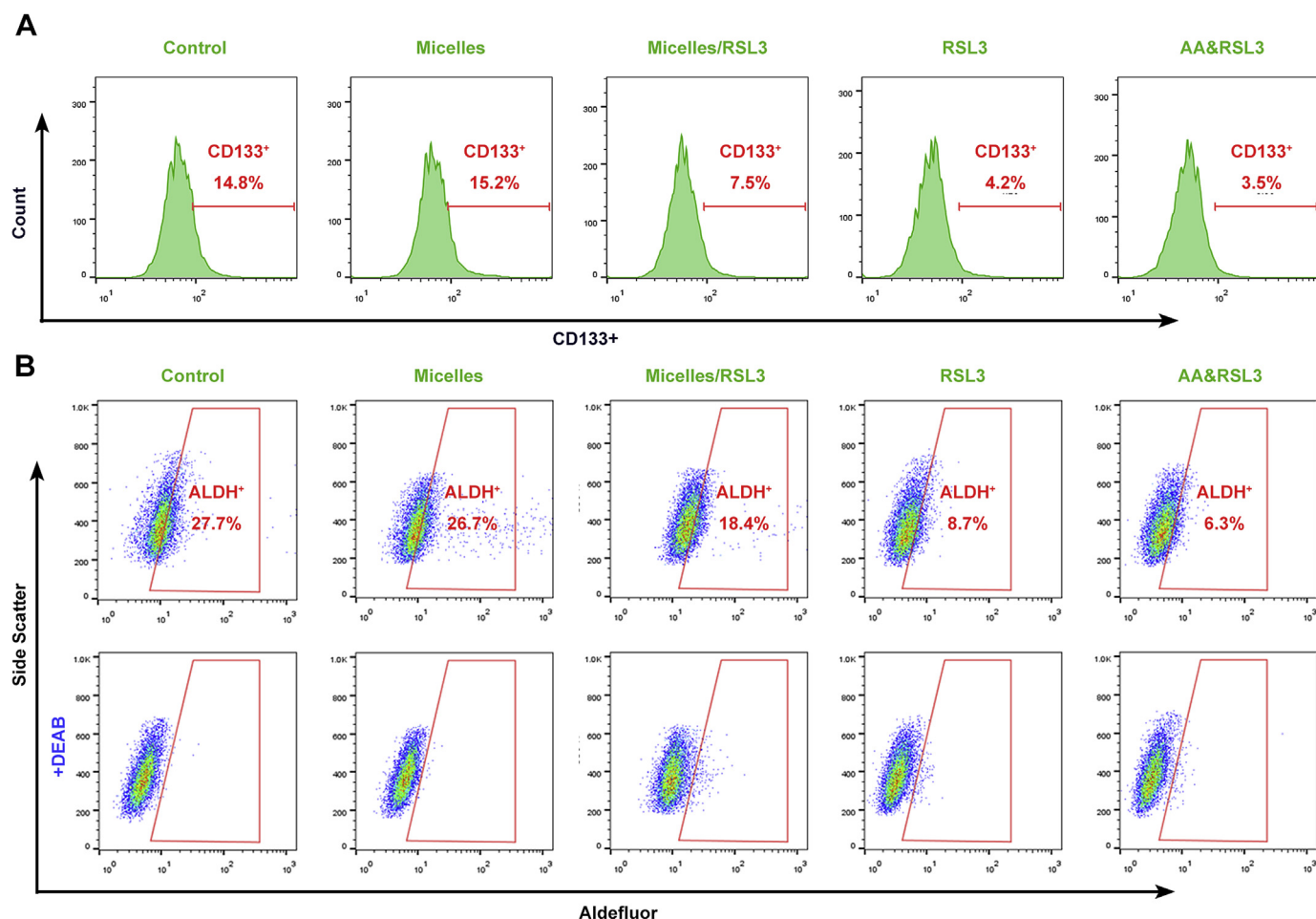


Fig. 4. Flow cytometry analysis of cancer stem cell subpopulation in NAR cells treated by four different formulations including activatable micelles, micelles/RSL3, free RSL3, and mixture of RSL3 and arachidonic acid (AA&RSL3). (A) The CD133⁺ cell subpopulation; (B) The ALDH⁺ cell subpopulation; the Aldefluor-positive cell population were selected with reference to a negative control (+DEAB, lower panel).

pharmacological effect [51]. Therefore, the extent of micelles accumulation in the tumor site is essential for a satisfactory therapeutic outcome. The EPR effect-based targeting strategy has been reported to only deliver ca. 1% administered dose to the tumor site [52,53]. Moreover, the majority of non-covalent nanoencapsulation method could only load limited (< 5%) amount of payloads in the nanocarrier [54,55]. Since it has been very challenging to enhance passive targeting efficiency [56], the concept of triggered all-active nanomedicine could fully utilize the nanocarrier that was deposited in the tumor site [24]. Thus, an enhanced therapeutic efficacy was expected using the ROS-responsive micelles for triggered delivery of RSL3.

3.6. RSL3-loaded micelles enhanced the therapeutic efficacy in NAR-grafted mice

Analogous to the cell viability study (Fig. 5), the ROS-responsive micelles/RSL3 achieved the best *in vivo* anti-tumor performance among the five tested formulations in the current study (Fig. 7A). Phosphate buffered saline (PBS) as the negative control ranked at the bottom in terms of antitumor efficacy. Free AA&RSL3 or RSL3 was inferior to the micelles/RSL3 as a consequence of their poor tumor targeting ability. Activatable micelles displayed low potency in inhibiting tumor growth because of the low extent of ferroptosis involvement. The potency of RSL3-loaded micelles in reducing resistant tumor cells arose from the following factors: 1) RSL3-induced ferroptosis and subsequent imbalance of redox homeostasis for efficient PCCs removal; 2) ROS-triggered rapid payload release; 3) AA-mediated GSH depletion to enhance

the action of ferroptosis as an assistant. In the end of efficacy study, the mass of remaining tumor coincided well with the tumor growth inhibition curve (Fig. 7C). For all groups, the mice body weight almost remained constant within the first three weeks, followed by a slight decrease (Fig. 7B). The histological staining analysis of the major healthy organs in the end of therapy indicated the absence of serious adverse effects (Fig. S4, Supporting Information). The mice survival curve also concurred well with the tumor growth inhibition profile; the micelles/RSL3 significantly extended the survival rate of NAR tumor-bearing mice compared to other formulations (Fig. 7D). These exciting results were thought because of the superb ability of all-active micelles/RSL3 in GPX4 inhibition and ferroptosis induction (Fig. 7E). The capability of ROS-responsive ferroptotic micelles in eliminating PCCs was proved by the analysis of the subpopulation of CD133⁺/ALDH⁺ cells in the tumor tissue at 48 h post the first dosing (Fig. 7F and G). This trend is partly consistent with *in vitro* biomarker analysis; the passive tumor targeting of micelles via EPR effect dramatically boosted the *in vivo* ability in terms of PCCs elimination. The histological tumor tissue analysis in the end of efficacy study also supported the anti-tumor potency of triggered ferroptotic micelles (Fig. 7H).

4. Conclusion

Since PCCs were believed as one important reason for drug resistance in traditional antitumor chemotherapy, we proposed that the ferroptosis-based programmed cell death mechanism could well address this issue by manipulating intracellular redox homeostasis and

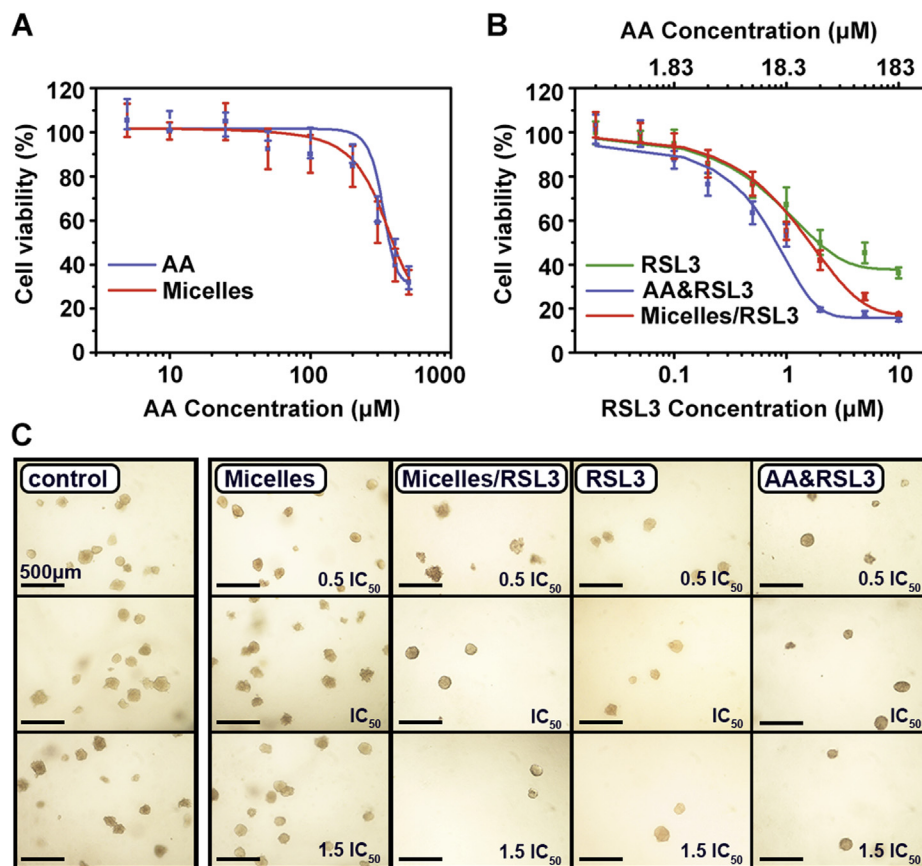


Fig. 5. The cellular viability and colony forming assay of NAR cells in response to different formulations treatment (n = 5). (A) Free AA and activatable micelles; (B) Free RSL3, AA&RSL3, and micelles/RSL3; (C) Optical images of NAR cell colonies in soft agar post formulation treatment at different dose (scale bar: 500 μm).

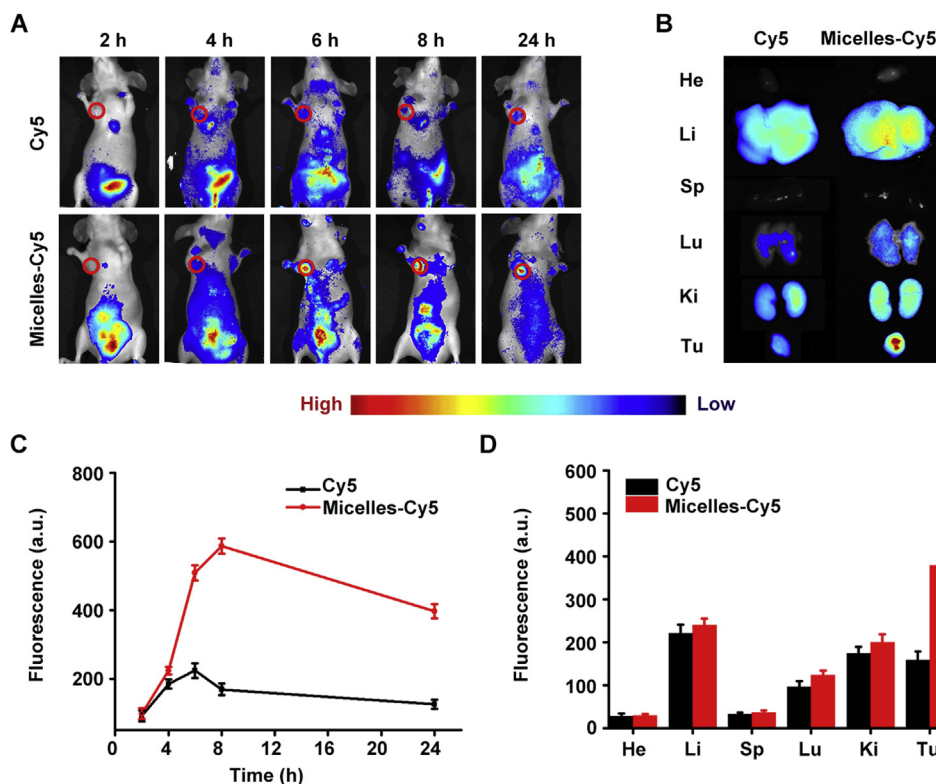


Fig. 6. Biodistribution of free Cy5 and Cy5-labelled micelles in NAR tumor-bearing nude mice (n = 3). (A) The *in vivo* kinetic accumulation of Cy5 after intravenous administration. (B) Fluorescent semi-quantification of Cy5 in excised tumor and major organs at 24 h post dosing. (C) Comparison of kinetic fluorescent intensity of Cy5 in tumor site between mice treated by free Cy5 and Cy5 labelled micelles (n = 3). (D) Fluorescent intensity of Cy5 in excised tumor and major organs at 24 h post dose administration (n = 3). Heart (He), Liver (Li), Spleen (Sp), Lung (Lu), Kidney (Ki), Tumor (Tu).

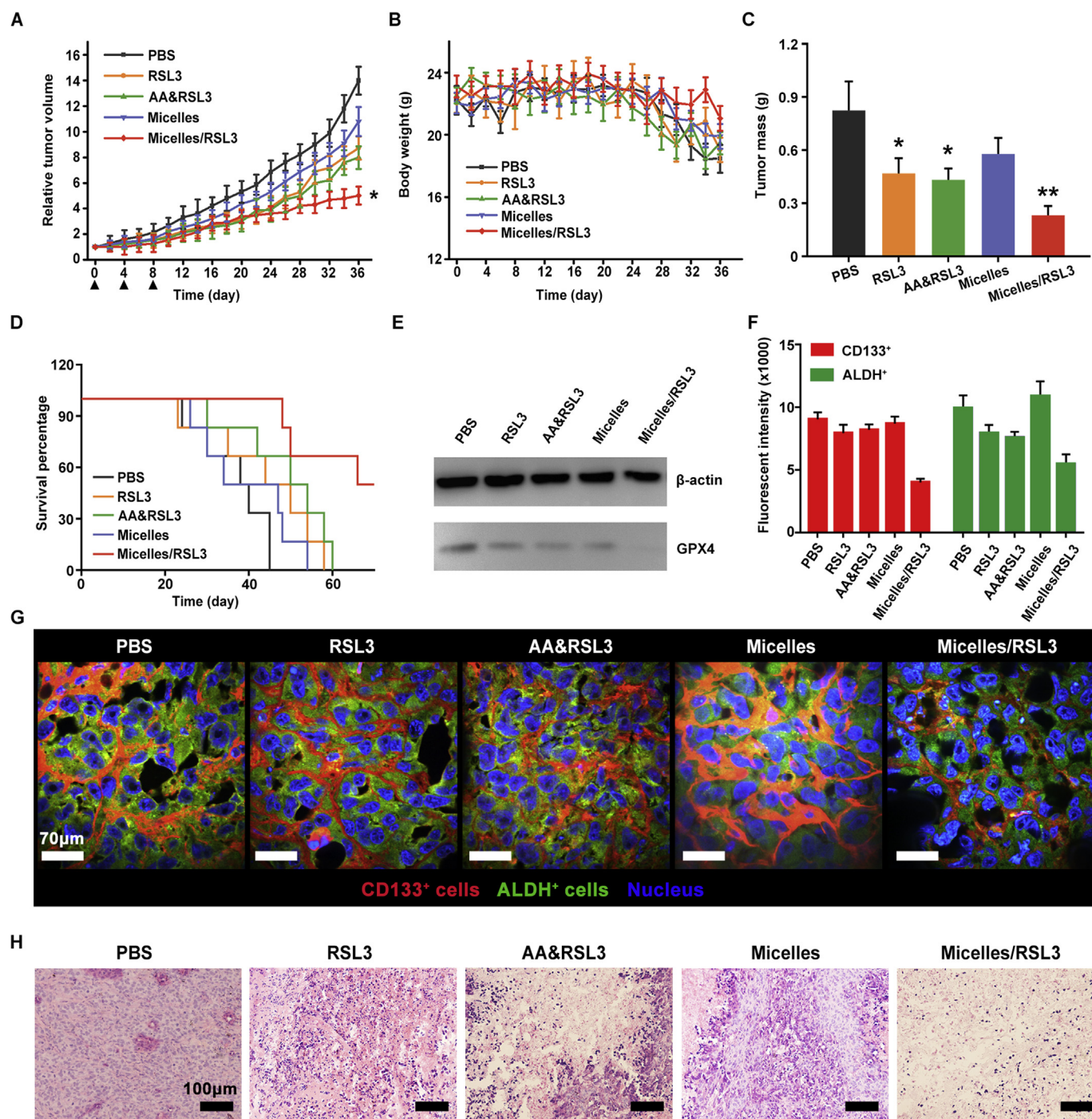


Fig. 7. *In vivo* antitumor performance of different formulations in NAR tumor-bearing nude mice. (A) Tumor growth curves of different groups treated by five formulations (PBS, free RSL3, AA&RSL3, activatable micelles, and micelles/RSL3); (B) Kinetic variation of body weight of mice during the treatment; (C) Quantitative analysis of tumor mass on the 36th day post the first dosing; (D) Kaplan–Meier mice survival curve; (E) Western blotting images of GPX4 expression in tumor tissues 48 h post treatment initiation; (F) Fluorescent intensities of CD133⁺ and ALDH⁺ cells in the tumor tissues 48 h post treatment initiation; (G) Immunofluorescent staining of CD133⁺ and ALDH⁺ cells in the tumor tissue 48 h post treatment initiation; (H) Histological analysis of tumor tissue by H&E staining. The data are presented mean \pm standard deviation (n = 6), **p* < 0.05, ***p* < 0.01.

eliminating quiescent PCCs. Such concept was further integrated with the unsaturated lipids-bearing triggered antitumor micelles to enable triggered rapid cargo release, GSH depletion, and hence enhanced ferroptotic cell death. Efficient PCCs elimination by ferroptosis was observed both *in vitro* in DOX-resistant NAR cells and *in vivo* in NAR tumor-bearing nude mice. The current work assembled ferroptosis-mediated PCCs diminishment, triggered micelles, and intracellular GSH depletion in one tailored nanoplatform. Such proof-of-concept can be

applied to a broad variety of resistant tumors as a potential treatment modality to avoid or prevent tumor relapse.

Author contributions

The manuscript was written through contributions of all authors. All authors have given approval to the final version of the manuscript. Gao M and Deng J contributed equally to this work.

Notes

The authors declare no competing financial interest.

Data availability

The raw/processed data required to reproduce these findings cannot be shared at this time due to technical or time limitations. However, upon request, these information are available from the corresponding author.

Acknowledgment

We acknowledge the funding support from the National Basic Research Program of China (2015CB856500), and the Tianjin Research Program of Application Foundation and Advanced Technology (18JCZDJC35700).

Appendix A. Supplementary data

Supplementary data to this article can be found online at <https://doi.org/10.1016/j.biomaterials.2019.119486>.

References

- G. Szakacs, J.K. Paterson, J.A. Ludwig, C. Booth-Genthe, M.M. Gottesman, Targeting multidrug resistance in cancer, *Nat. Rev. Drug Discov.* 5 (2006) 219–234.
- P.B. Gupta, C.L. Chaffer, R.A. Weinberg, Cancer stem cells: mirage or reality? *Nat. Med.* 15 (2009) 1010–1012.
- D. Nassar, C. Blanpain, Cancer stem cells: Basic concepts and therapeutic implications, *Ann. Rev. Pathol.* 11 (2016) 47–76.
- Y. Zhao, D.Y. Alakhova, A.V. Kabanov, Can nanomedicines kill cancer stem cells? *Adv. Drug Deliv. Rev.* 65 (2013) 1763–1783.
- H. Clevers, The cancer stem cell: premises, promises and challenges, *Nat. Med.* 17 (2011) 313–319.
- E. Battle, H. Clevers, Cancer stem cells revisited, *Nat. Med.* 23 (2017) 1124–1134.
- R. Sato, T. Semba, H. Saya, Y. Arima, Concise review: stem cells and epithelial-mesenchymal transition in cancer: biological implications and therapeutic targets, *Stem Cells* 34 (2016) 1997–2007.
- G.J. Yoshida, H. Saya, Therapeutic strategies targeting cancer stem cells, *Cancer Sci.* 107 (2016) 5–11.
- T. Shibue, R.A. Weinberg, EMT, CSCs, and drug resistance: the mechanistic link and clinical implications, *Nat. Rev. Clin. Oncol.* 14 (2017) 611–629.
- V.S. Viswanathan, M.J. Ryan, H.D. Dhruv, S. Gill, O.M. Eichhoff, B. Seashore-Ludlow, et al., Dependency of a therapy-resistant state of cancer cells on a lipid peroxidase pathway, *Nature* 547 (2017) 453–457.
- M.J. Hangauer, V.S. Viswanathan, M.J. Ryan, D. Bole, J.K. Eaton, A. Matov, et al., Drug-tolerant persister cancer cells are vulnerable to GPX4 inhibition, *Nature* 551 (2017) 247–250.
- T.T. Mai, A. Hamai, A. Hienzsch, Salinomycin kills cancer stem cells by sequestering iron in lysosomes, *Nat. Chem.* 9 (2017) 1025–1033.
- S.J. Dixon, K.M. Lemberg, M.R. Lamprecht, R. Skouta, E.M. Zaitsev, C.E. Gleason, et al., Ferroptosis: an iron-dependent form of nonapoptotic cell death, *Cell* 149 (2012) 1060–1072.
- B.R. Stockwell, J.P. Friedmann Angeli, H. Bayir, A.I. Bush, M. Conrad, S.J. Dixon, et al., Ferroptosis: a regulated cell death nexus linking metabolism, redox biology, and disease, *Cell* 171 (2017) 273–285.
- V.E. Kagan, G. Mao, F. Qu, J.P. Angeli, S. Doll, C.S. Croix, et al., Oxidized arachidonic and adrenic PEs navigate cells to ferroptosis, *Nat. Chem. Biol.* 13 (2017) 81–90.
- S.E. Wenzel, Y.Y. Tyurina, J. Zhao, C.M. St Croix, H.H. Dar, G. Mao, et al., PEBP1 warden ferroptosis by enabling lipoxygenase generation of lipid death signals, *Cell* 171 (2017) 628–641.
- A.J. Rennekamp, The ferrous awakens, *Cell* 171 (2017) 1225–1227.
- D.W. Zheng, Q. Lei, J.Y. Zhu, J.X. Fan, C.X. Li, C. Li, et al., Switching apoptosis to ferroptosis: metal-organic network for high-efficiency anticancer therapy, *Nano Lett.* 17 (2017) 284–291.
- W. Ou, R.S. Mulik, A. Anwar, J.G. McDonald, X. He, I.R. Corbin, Low-density lipoprotein docosahexaenoic acid nanoparticles induce ferroptotic cell death in hepatocellular carcinoma, *Free Radic. Biol. Med.* 112 (2017) 597–607.
- D. Peer, J.M. Karp, S. Hong, O.C. Farokhzad, R. Margalit, R. Langer, Nanocarriers as an emerging platform for cancer therapy, *Nat. Nanotechnol.* 2 (2007) 751–760.
- M. Gao, C. Chen, A. Fan, J. Zhang, D. Kong, Z. Wang, et al., Covalent and non-covalent curcumin loading in acid-responsive polymeric micellar nanocarriers, *Nanotechnology* 26 (2015) 275101.
- D. Rosenblum, N. Joshi, W. Tao, Progress and challenges towards targeted delivery of cancer therapeutics, *Nat. Commun.* 9 (2018) 1410.
- H. Maeda, Toward a full understanding of the EPR effect in primary and metastatic tumors as well as issues related to its heterogeneity, *Adv. Drug Deliv. Rev.* 91 (2015) 3–6.
- M. Gao, X. Meng, X. Guo, J. Zhu, A. Fan, Z. Wang, et al., All-active antitumor micelles via triggered lipid peroxidation, *J. Control. Release* 286 (2018) 381–393.
- K. Yamanaka, Y. Saito, J. Sakiyama, Y. Ohuchi, F. Oseto, N. Noguchi, A novel fluorescent probe with high sensitivity and selective detection of lipid hydroperoxides in cells, *RSC Adv.* 2 (2012) 7894–7900.
- X. Hu, X. Jing, Biodegradable amphiphilic polymer-drug conjugate micelles, *Expert Opin. Drug Deliv.* 6 (2009) 1079–1090.
- V.P. Torchilin, Micellar nanocarriers: pharmaceutical perspectives, *Pharm. Res.* 24 (2007) 1–16.
- X. Meng, M. Gao, J. Deng, D. Lu, A. Fan, D. Ding, et al., Self-immolative micellar drug delivery: the linker matters, *Nano Res* 11 (2018) 6177–6189.
- X. Huang, D. Lu, Y. Ma, L. Zhang, L. Wang, J. Deng, et al., From small deferiprone to macromolecular micelles: self-assembly enhances iron chelation, *J. Colloid Interface Sci.* 533 (2019) 375–384.
- K. Park, Facing the truth about nanotechnology in drug delivery, *ACS Nano* 7 (2013) 7442–7447.
- Z. Wang, C. Chen, Q. Zhang, M. Gao, J. Zhang, D. Kong, et al., Tuning the architecture of polymeric conjugate to mediate intracellular delivery of pleiotropic curcumin, *Eur. J. Pharm. Biopharm.* 90 (2015) 53–62.
- C.W. Freudiger, W. Min, B.G. Saar, S. Lu, G.R. Holtom, C. He, et al., Label-free biomedical imaging with high sensitivity by stimulated Raman scattering microscopy, *Science* 322 (2008) 1857–1861.
- X. Li, M. Gao, K. Xin, L. Zhang, D. Ding, D. Kong, et al., Singlet oxygen-responsive micelles for enhanced photodynamic therapy, *J. Control. Release* 260 (2017) 12–21.
- W.S. Yang, R. SriRamaratnam, M.E. Welsch, K. Shimada, R. Skouta, V.S. Viswanathan, et al., Regulation of ferroptotic cancer cell death by GPX4, *Cell* 156 (2014) 317–331.
- M.M. Gaschler, A.A. Andia, H. Liu, J.M. Csuka, B. Hurlocker, C.A. Vaiana, et al., FINO₂ initiates ferroptosis through GPX4 inactivation and iron oxidation, *Nat. Chem. Biol.* 14 (2018) 507–515.
- G.Y. Liou, P. Storz, Reactive oxygen species in cancer, *Free Radic. Res.* 44 (2010) 479–496.
- D. Lu, R. Tao, Z. Wang, Carbon-based materials for photodynamic therapy: a mini-review, *Front. Chem. Sci. Eng.* 13 (2018) 310–323.
- P.L. Else, E. Kraffe, Docosahexaenoic and arachidonic acid peroxidation: it's a within molecule cascade, *Biochim. Biophys. Acta* 1848 (2015) 417–421.
- C. Peitzsch, A. Tyutyunnykova, K. Pantel, A. Dubrovka, Cancer stem cells: the root of tumor recurrence and metastasis, *Semin. Cancer Biol.* 44 (2017) 10–24.
- H. Dianat-Moghadam, M. Heidarifard, R. Jahanban-Esfahlan, Y. Panahi, H. Hamishehkar, F. Pouremamali, et al., Cancer stem cells-emanated therapy resistance: implications for liposomal drug delivery systems, *J. Control. Release* 288 (2018) 62–83.
- D. Burgos-Ojeda, B.R. Rueda, R.J. Buckanovich, Ovarian cancer stem cell markers: prognostic and therapeutic implications, *Cancer Lett.* 322 (2012) 1–7.
- Y. Tao, H. Li, R. Huang, D. Mo, T. Zeng, M. Fang, et al., Clinicopathological and prognostic significance of cancer stem cell markers in ovarian cancer patients: evidence from 52 studies, *Cell. Physiol. Biochem.* 46 (2018) 1716–1726.
- G. Liu, D. Jian, L. Fang, W. Zheng, D. Peer, Y. Zhao, Hierarchically theranostic nanomedicine: MRI Contrast agents as the physical vehicle anchor for high drug loading and triggered on-demand delivery, *J. Mater. Chem. B* 6 (2018) 1995–2003.
- K. Cohen, R. Emmanuel, E. Kisin-Finifer, D. Shabat, D. Peer, Modulation of drug resistance in ovarian adenocarcinoma using chemotherapy entrapped in hyaluronan-grafted nanoparticle clusters, *ACS Nano* 8 (2014) 2183–2195.
- H. Li, M. Li, C. Chen, A. Fan, D. Kong, Z. Wang, et al., On-demand combinational delivery of curcumin and doxorubicin via a pH-labile micellar nanocarrier, *Int. J. Pharm.* 495 (2015) 572–578.
- S. Borowicz, M. Van Scoyk, S. Avasarala, M.K. Karuppusamy Rathinam, J. Tauler, R.K. Bikkavilli, et al., The soft agar colony formation assay, *J. Vis. Exp.* 92 (2014) e51998.
- N.A. Franken, H.M. Rodermond, J. Stap, J. Haveman, C. van Bree, Clonogenic assay of cells in vitro, *Nat. Protoc.* 1 (2006) 2315–2319.
- V. Rajendran, M.V. Jain, In vitro tumorigenic assay: colony forming assay for cancer stem cells, *Methods Mol. Biol.* 1692 (2018) 89–95.
- R. Tao, M. Gao, F. Liu, X. Guo, A. Fan, D. Ding, et al., Alleviating the liver toxicity of chemotherapy via pH-responsive hepatoprotective prodrug micelles, *ACS Appl. Mater. Interfaces* 10 (2018) 21836–21846.
- H. Maeda, Macromolecular therapeutics in cancer treatment: the EPR effect and beyond, *J. Control. Release* 164 (2012) 138–144.
- E. Blanco, H. Shen, M. Ferrari, Principles of nanoparticle design for overcoming biological barriers to drug delivery, *Nat. Biotechnol.* 33 (2015) 941–951.
- Y.H. Bae, K. Park, Targeted drug delivery to tumors: myths, reality and possibility, *J. Control. Release* 153 (2011) 198–205.
- Y. Nakamura, M. Ai, P.L. Choyke, H. Kobayashi, Nano-drug delivery: is the enhanced permeability and retention (EPR) effect sufficient for curing cancer? *Bioconj. Chem.* 27 (2016) 2225–2238.
- K. Cai, X. He, Z. Song, Q. Yin, Y. Zhang, F.M. Uckun, et al., Dimeric drug polymeric nanoparticles with exceptionally high drug loading and quantitative loading efficiency, *J. Am. Chem. Soc.* 137 (2015) 3458–3461.
- S. Lv, Y. Wu, K. Cai, H. He, Y. Li, M. Lan, et al., High drug loading and sub-quantitative loading efficiency of polymeric micelles driven by donor-receptor co-ordination interactions, *J. Am. Chem. Soc.* 140 (2018) 1235–1238.
- A.J. Tavares, W. Poon, Effect of removing Kupffer cells on nanoparticle tumor delivery, *Proc. Natl. Acad. Sci. U.S.A.* 114 (2017) E10871–e10880.